

Dynamic Behavior of Ribbed Viscoelastic CNT-PDMS Thin-Films for Multifunctional Applications

Matthew Phillips, Muh-Jang Chen, Jong Ryu, and Mohammed Zikry*

Tailored ribbing structures are obtained by large-scale rolling in polymer PDMS thin-films by adding carbon nanotubes (CNT) inclusions, which significantly improved the mechanical behavior of systems subjected to dynamic compressive strain rates. A nonlinear explicit dynamic three-dimensional finite-element (FE) scheme is used to understand and predict the thermomechanical response of the manufactured ribbed thin-film structures subjected to dynamic in-plane compressive loading. Representative volume element (RVE) FE models of the ribbed thin-films are subjected to strain rates as high as 10⁴ s⁻¹ in both the transverse and parallel ribbing directions. Latin Hypercube Sampling of the microstructural parameters, as informed from experimental observations, provide the microstructurally based RVEs. An interior-point optimization routine is also employed on a regression model trained from the FE predictions that can be used to design ribbed materials for multifunctional applications. The model verifies that damage can be mitigated in CNT-PDMS systems subjected to dynamic compressive loading conditions by controlling the ribbing microstructural characteristics, such as the film thickness and the ribbing amplitude and wavelength. This approach provides a framework for designing materials that can be utilized for applications that require high strain rate damage tolerance, drag reduction, antifouling, and superhydrophobicity.

1. Introduction

Thin-film systems can be tailored for multifunctional applications, and the surface topology of the thin-film plays a significant role in behavior, such as superhydrophobicity,[1-7] anti-icing, [2,7] anti-fouling, [8,9] self-cleaning, [10] optical, [8,9] or electrical.[8,9,11-14] Different manufacturing approaches to obtain these surface behaviors have been undertaken, such as plasma^[1]

M. Phillips, M.-J. Chen, J. Ryu, M. Zikry Department of Mechanical and Aerospace Engineering North Carolina State University Raleigh, NC 27695, USA E-mail: zikry@ncsu.edu

The ORCID identification number(s) for the author(s) of this article can be found under https://doi.org/10.1002/mame.202400098

© 2024 The Author(s). Macromolecular Materials and Engineering published by Wiley-VCH GmbH. This is an open access article under the terms of the Creative Commons Attribution License, which permits use, distribution and reproduction in any medium, provided the original work

DOI: 10.1002/mame.202400098

or abrading^[2] treatments of thin polymer or ceramic sheets, photolithography^[12] or roller embossing,[3,5] and inducing wrinkling topologies. [8,11,13–15] Some of these surface treatments, however, do not produce consistent surfaces, and others require expensive or complex processing and manufacturing approaches. Lithography-free techniques, such as large-scale rolling or wrinkling, do not require time-consuming processing or complex manufacturing approaches to create surface features with high aspect ratios.[4,6,8,16] Wrinkled surfaces, for example, are typically produced by compressing and permanently deforming the thin-film to the desired hierarchal surface structure. These lithography-free techniques can also allow for the control of the wavelength, the amplitude, and the orientation of desired topologies or patterns, and these surface characteristics can be directly linked to material properties and manufacturing conditions.[8,11,13-15,17]

Topologies, such as ribbed surfaces, have desirable multifunctional applications.[4,6,16] Ribbing structures are

periodic surfaces that are generated by large-scale rolling, which allows for continuous, template-free manufacturing. These finger-like periodic structures develop in the meniscus between the two separating surfaces when the Capillary number, Ca = $\mu U/\gamma$, exceeds a critical value where μ is the viscosity, U is the characteristic speed, and γ is the surface energy of the material. [4,6,18-23] Although most approaches have viewed material ribbing as defects, and the general approach has been to minimize their generation,[18-28] there are advantageous behaviors, such as drag reduction, anti-biofouling, self-cleaning, superhydrophobicity, and anti-icing^[4–6,16] that can be obtained with ribbed structures. Furthermore, roll-to-roll manufacturing processing have been used and proposed for the development of structured materials for use in fuel cells, batteries, and multifunctional thin-films.[29]

Large-scale, roll-to-roll manufacturing of ribbed thin-films provides the ability to control the topology by varying the manufacturing conditions and material properties of the film. [5,6,16,30] CNT-PDMS material systems are a potentially desirable system because the viscoelasticity of the uncured PDMS increases the Capillary number, which is directly related to the generation of ribbing structures during large-scale rolling. The high



www.mame-journal.de

aspect ratio CNT inclusions provide strength to retain the periodic structure, such that it can be cured, and the high aspect ratio of the CNTs increase the achievable surface texture necessary for superhydrophobicity and drag reduction surface behaviors. There are other benefits to adding CNT or other such carbon-based and nano-sized inclusions in a polymer matrix, such as increased stiffness and strength,[31-35] increased thermal and electrical conductivity,[33,35-37] improved thermal stability,[38] and flame retardant capabilities, [37] which can make these composite systems ideal for flexoelectric, piezoelectric, and other multifunctional applications. For these materials to be beneficial for multifunctional applications, however, it is important to understand the influence of the filler size, orientation, dispersion, and interface with the matrix material on the effective properties of the heterogeneous systems. Analytical, [39-41] experimental,[41] and computational[39,42-46] approaches have been used to account for these factors with CNT-polymer systems.

While the effective properties of CNT-PDMS materials and the manufacturing of ribbed CNT-PDMS structures is understood, there is little or no understanding how the structured material responds to extreme conditions that may be encountered while in-use, such as high strain rate loading conditions. Experimental investigations have been conducted on thin polymer^[47–49] and metal[33,50-52] films to understand how high strain rate behavior affects thin-films for such applications as MEMS devices, among others. Thermo-viscoelastic materials are particularly sensitive to extreme conditions because the temperature dependence and loading history of the material significantly change the system's ability to dissipate energy and inhibit failure modes, such as dynamic fracture. This is apparent in systems, such as rubberlike tires, where cyclic deformation results in heating of these viscoelastic materials^[48] thereby softening and altering the energy absorption. Similarly, highly stretchable strain sensors constructed from a PDMS matrix with aligned CNT inclusions exhibits hysteresis during cyclic loading, resulting from the viscoelasticity of the matrix, which aids the device in enduring cycles of high dynamic strains with minimal damage.[49] For these structured thin-films to be functional, there must be a fundamental understanding of the dynamic behavior and damageresistance when subjected to extreme environments of high strain-rates.

Hence, a computational framework is needed to predict the relation between the viscoelastic material properties and ribbing morphology on the thermomechanical response for structured thin-films subjected to dynamic strain rates. The major goal of this investigation, therefore, is to evaluate the response of structured CNT-PDMS thin-film materials subjected to in-plane dynamic compressive loading conditions, and to understand and predict the thermomechanical behavior of these films to highstrain rate extreme conditions. Furthermore, design recommendations are developed to optimize thermomechanical behavior by tailoring the ribbing morphology of thin-films. This work is organized as follows: in Section 2 the theory of the thermo-rheological viscoelastic material model is detailed then the morphology of ribbing structures is explained; in Section 3, the FE modeling approach is described; in Section 4, the thermomechanical thin-film results are presented and discussed; and in Section 5, a summary is outlined.

2. CNT-PDMS Rheometry and Thin-Film Ribbing Behavior

2.1. Viscoelastic Material Model of the CNT-PDMS Paste Formulations

The mechanical behavior of cured CNT-PDMS can be modeled as a viscoelastic material because the polymer chains exhibit timeor rate-dependent relaxation. [4,16,53] Prony series viscoelastic material models have been used to represent the relaxation behavior as a function of time or frequency. [16,53–56] An n-term Prony series model for the shear storage, $G'(\omega)$, and the loss moduli, $G''(\omega)$, of a material are given as a function of angular frequency (ω) ,

$$G'(\omega) = G_0 \sum_{i=1}^{n} \frac{g_i \tau_i^2 \omega^2}{1 + \tau_i^2 \omega^2} + G_{\infty}$$
 (1)

and

$$G''(\omega) = G_0 \sum_{i=1}^n \frac{g_i \tau_i \omega}{1 + \tau_i^2 \omega^2}$$
 (2)

where G_0 is the instantaneous shear modulus, G_{∞} is the long-term shear modulus, and g_i are the dimensionless relaxation coefficients corresponding to the time constants τ_i . The Prony series representation of the shear modulus in the time-domain, G(t), is

$$G(t) = G_0 \sum_{i=1}^{n} g_i e^{-\frac{t}{\tau_i}} + G_{\infty}$$
 (3)

with the same constants and coefficients as in the frequency domain. ^[54] In some formulations, such as the simplified Universal Polymer Model (UPM), ^[53,57] G_{∞} is specified directly and requires that the summation of relaxation coefficients equals unity. In the present study, the long-term shear modulus is not specified directly, but rather is obtained by

$$G_{\infty} = G_0 \left(1 - \sum_{i=1}^n g_i \right) \tag{4}$$

where the summation of g_i is less than unity. The frequency- or time-dependent elongation modulus behavior can be obtained from the shear modulus behavior assuming a constant Poisson ratio.

2.2. Thermo-Rheological Behavior of CNT-PDMS

Since inelastic heat generation is considered for the dynamic loading conditions, the temperature of the material is anticipated to increase, thereby softening the material. This softening can be accounted for by the time-temperature superposition principle. The Williams–Landel–Ferry (WLF) model accounts for the temperature effects by the log-scale horizontal shift factor, a_T , given by

$$\log a_T = -\frac{C_1(T - T_0)}{C_2 + (T - T_0)} \tag{5}$$

where C_1 and C_2 are fitting coefficients and T_0 is some arbitrary reference temperature, typically given as room temperature or near the glass transition temperature. [54,56–58] The shift factor

14392054, 0, Downloaded from https://onlinelibrary.wikey.com/doi/10.1002/mame.202400098 by North Carolina State Universit, Wiley Online Library on [30/09/2024]. See the Terms and Conditions (https://onlinelibrary.wiley.com/terms-and-conditions) on Wiley Online Library for rules of use; OA articles are governed by the applicable Creative Commons Licesson

www.mame-journal.de

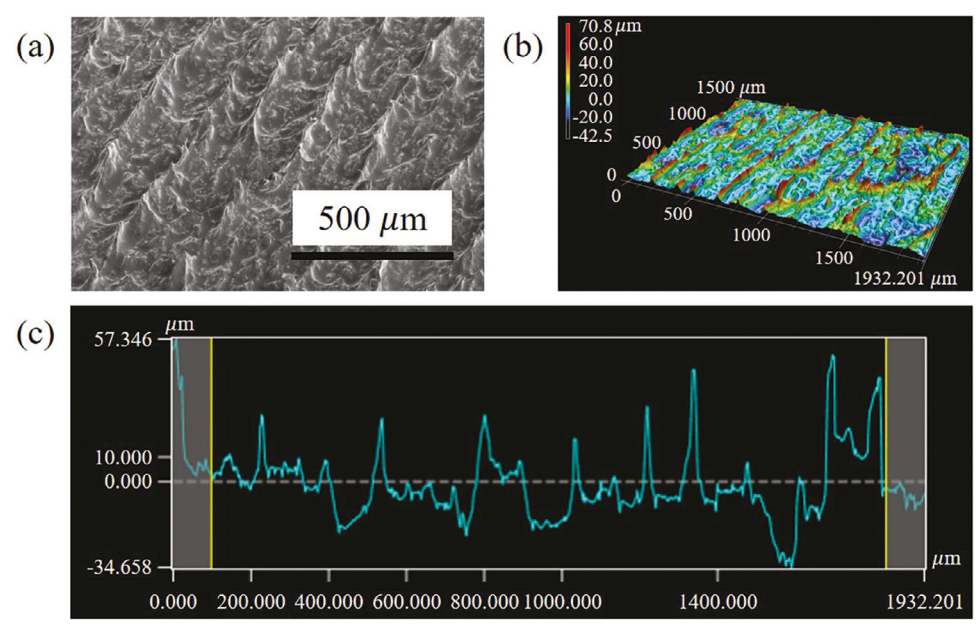


Figure 1. a) Scanning electron microscope (SEM) image, b) optical microscopy image, and c) morphological characterization from optical microscopy imaging of CNT-PDMS ribbing structures.

modifies the frequency-dependent shear moduli at a given temperature with respect to the reference temperature by the relation $G'(\omega, T) = G'(a_T\omega, T_0)$ and $G''(\omega, T) = G''(a_T\omega, T_0)$; the time-dependent modulus is shifted by $G(t, T) = G(t/a_T, T_0)$. [54]

film stress that accumulates during the rolling process. Similarly, a second non-dimensional microstructural parameter can be introduced that describes the ratio of the film thickness to the ribbing wavelength, called the ribbing length ratio ($\alpha_l = H/\lambda$).

2.3. Ribbing Morphology of Thin-Films

Ribbing structures are periodic surfaces that can develop in thin liquid and solid films during manufacturing processes, such as large-scale rolling. The morphology of the periodic structure can be characterized by a ribbing amplitude (A) and ribbing wavelength (λ) because the surface often rearranges into a uniform linear pattern along the rolling direction under certain conditions.^[4,6] The thickness (H) of ribbed thin-films can also be controlled by the manufacturing conditions.^[4,16] These parameters can be observed by scanning electron microscopy (SEM) or optical microscopy (**Figure 1**).

A parametric large-scale rolling study was conducted in refs. [4, 16] using PDMS with 3.5 wt% CNT to determine the effect that the roller gap has on the resulting ribbing microstructure. By adding CNT inclusions to the PDMS matrix, the viscosity of the material increased such that it retained the ribbing structure after rolling and allowed for the thermoset material to be cured. The addition of CNTs also decreased the achievable wavelength compared to neat PDMS. SEM measurements (Figure 1) provide detailed microstructural characteristics after the PDMS was cured.

A non-dimensional ribbing microstructural parameter, the ribbing aspect ratio (α_r), was introduced in ref. [16] to characterize the asperity of the ribbing structure, defined as the ribbing amplitude divided by the ribbing wavelength ($\alpha_r = A/\lambda$). The feature aspect ratio is also used to characterize other such systems as wrinkled thin-films and structured topographical surfaces. [8.59] Based on ref. [16] α_r can be used to understand and predict the

3. 3D Finite-Element (FE) Approach

The Prony series viscoelastic material model and the ribbing microstructural measurements were used with a nonlinear explicit dynamic computational scheme to investigate the dynamic behavior of CNT-PDMS thin-film systems subjected to in-plane compressive loading. A fully coupled thermal-stress explicit analysis was conducted to evaluate the dynamic response and account for the thermo-rheological behavior of the material and the inelastic heat generation that will result from viscoelastic energy dissipation. The mechanical solution is obtained using an explicit central-difference integration scheme with a lumped mass matrix; the heat dissipation equations are solved using a first-order explicit forward-difference time integration rule with a lumped capacitance matrix. The stable time increment for the mechanical response is $\Delta t \approx \frac{L_{min}}{c_d}$ where L_{min} is the smallest element dimension and c_d is the current dilatation wave speed defined by $c_d = \sqrt{\frac{\lambda + 2\mu}{\rho}}$ where the Lame's constants are determined in the current dilatation wave speed mined at the current time-step based on the mean and incremental stresses and strains. Similarly, the stable time increment for the thermal response is $\Delta t \approx \frac{\dot{L}_{min}^2}{2\alpha}$ where $\alpha = \frac{k}{\rho c}$ and ρ is the density, k is the thermal conductivity, and c is the specific heat.[54]

The CNT-PDMS material was assumed to have homogeneous, isotropic material properties resulting from the mixing procedure. The material was assumed to exhibit similar mechanical relaxation behavior as neat PDMS. The Prony series relaxation

and Conditions (https://onlinelibrary.wiley.com/terms-and-conditions) on Wiley Online Library for rules of use; OA articles are governed by the applicable Creative Commons License

www.mame-journal.de

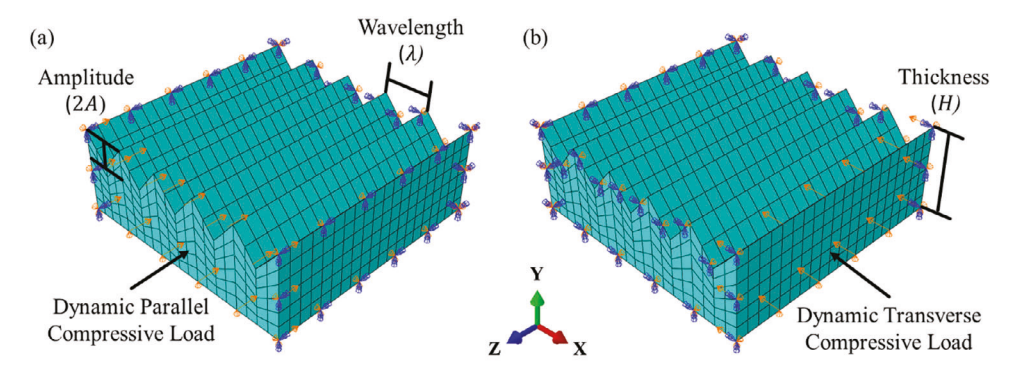


Figure 2. A representative volume element thin-film model subjected to a dynamic compressive load (a) parallel to the ribbing direction and b) transverse to the ribbing direction. Each thin-film model has a prescribed ribbing amplitude (λ), ribbing wavelength (λ), and film thickness (H) specified from the 16 microstructural combinations resulting from the Latin Hypercube Sampling routine. The bottom surface was simply supported, a dynamic compressive load was applied to one in-plane face, and symmetry boundary conditions were applied to the remaining in-plane faces.

behavior was obtained from ref. [53] for neat PDMS; the instantaneous modulus was obtained by rule of mixtures and a constant Poisson ratio, ν , of 0.48 was used. The WLF coefficients, C_1 , C_2 , and T_0 , were also obtained from ref. [53] to describe the time-temperature superposition according to Equation (5), with a density of $\rho = 989.5$ kg m³, thermal conductivity of 0.15 W m⁻¹ K⁻¹, and specific heat of 1460 J kg⁻¹ K⁻¹.

Three microstructural parameters were used to gain further fundamental understanding of how the microstructure evolved due to the three-dimensional dynamic loading conditions. These were the ribbing amplitude, ribbing wavelength, and film thickness. To understand the relation between the microstructure and the thermomechanical response to dynamic loading, a population of 16 RVE thin-film models with varying ribbing microstructures informed by experimental observations was introduced. The dynamic response of each RVE subjected to in-plane compressive loading for both neat PDMS and CNT-PDMS material properties were investigated to also understand how the addition of CNT inclusions in the PDMS matrix influences the thermomechanical behavior.

Two thousand four hundred 3D 8-node linear brick elements with full integration were used based on a convergence analysis to model the thermomechanical response of the thin-film. Five sinusoidal ribbing periods as a function of the film width were modeled for each RVE with the same mesh structure: four elements per wavelength and six elements tall. Each RVE was subjected to an in-plane dynamic compressive load in the direction of the ribbing structure (parallel load) and in the other in-plane direction (transverse load). Symmetry boundary conditions were applied to the remaining in-plane faces. The bottom surface was simply supported and the top surface was free. An initial temperature of 298 K was prescribed on all nodes. The mesh and prescribed boundary conditions of one RVE is shown in Figure 2.

Based on the material properties and mesh characteristics, the approximate stable time step for the mechanical and thermal solutions were obtained. For example, the stable time increment for neat PDMS is 10^{-7} s for the purely mechanical load and 10^{-3} s for the purely thermal load. Three strain rates were modeled for each of the loading directions: 10^2 , 10^3 , and 10^4 s⁻¹. The stable time-step was 10^{-7} s for 10^2 s⁻¹, 10^{-8} s for 10^3 s⁻¹, and 10^{-9} for 10^4 s⁻¹. The ramp times were 10^{-4} , 10^{-4} , 10^{-5} , and 10^{-6} s.

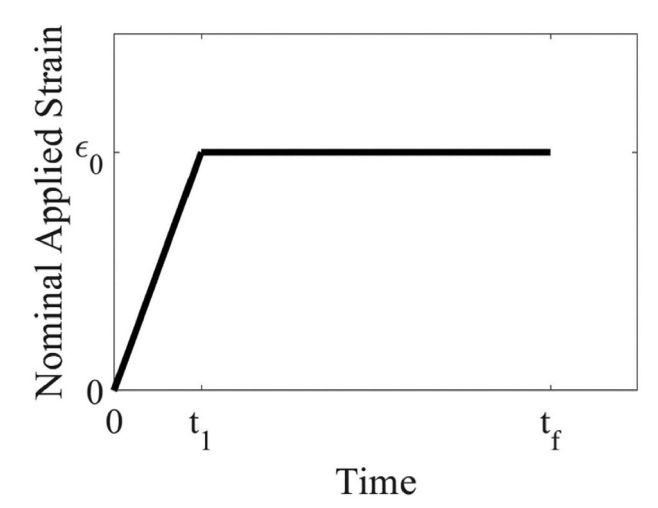


Figure 3. The magnitude of the dynamic compression loading for all representative volume element thin-film models. The ramp time, t_1 , was determined from the nominal strain rate. The final time, t_f , was set as 10 times the ramp time ($t_f = 10t_1$).

The total time that the dynamic behavior of each RVE was ten times the ramp time (**Figure 3**).

4. Results and Discussion

The proposed ribbing microstructure and FE computational approach were used to investigate the dynamic response of ribbed homogeneous PDMS and heterogeneous CNT-PDMS thin-films to compressive loads at various strain rates. The material model of the cured and neat PDMS and CNT-PDMS was obtained from ref. [53] and adapted for use in the 3D FE models. The population of 16 RVEs was used to predict the thermomechanical behavioral differences resulting from the microstructure, material properties, and nominal strain rates. Hypersurfaces of the thermomechanical response were developed to visualize the effect that the ribbing microstructure had for each nominal strain rate. A validated regression model of the characteristic response was also obtained from the hypersurfaces to predict and optimize the



www.mame-journal.de

Table 1. The 20-term Prony series characterization for cured, neat PDMS with time constants, τ_i , and relaxation coefficients, g_i , based on ref. [53] for the Universal Polymer Model (UPM) and recharacterized for use in 3D finite element models (FEM).

Prony Number i	Time Constant τ_i (s)	Relaxation Coefficient, g _i	
		UPM	3-D FEM
1	1.00 E-6	0.5061	0.3889
2	3.16 E-6	0.0000	0.0000
3	1.00 E-5	0.1276	0.0981
4	3.16 E-5	0.0755	0.0581
5	1.00 E-4	0.0661	0.0508
6	3.16 E-4	0.0568	0.0437
7	1.00 E-3	0.0420	0.0323
8	3.16 E-3	0.0356	0.0274
9	1.00 E-2	0.0258	0.0198
10	3.16 E-2	0.0190	0.0146
11	1.00 E-1	0.0126	0.0097
12	3.16 E-1	0.0110	0.0084
13	1.00 E+0	0.0040	0.0031
14	3.16 E+0	0.0062	0.0047
15	1.00 E+1	0.0023	0.0017
16	3.16 E+1	0.0029	0.0022
17	1.00 E+2	0.0020	0.0016
18	3.16 E+2	0.0017	0.0013
19	1.00 E+3	0.0009	0.0007
20	3.16 E+3	0.0018	0.0014

microstructure for design purposes when subjected to extreme high strain rate conditions.

4.1. PDMS and CNT-PDMS Viscoelastic Material Model

The material model^[53] for cured, neat PDMS was given according to Equation (3) with the sum of relaxation coefficients, g_i , equal to unity based on the UPM.^[57] The relaxation coefficients were rescaled to be less than unity for use in the 3D FE material model because the long-term shear modulus is not specified directly and instead is obtained by Equation (4). These time constants and associated relaxation coefficients for the 20-term Prony series are given in Table 1.

The instantaneous shear modulus, G_0 , of neat PDMS was 3.62 MPa. The relaxation coefficients were scaled such that the long-term shear modulus, G_{∞} , was 0.84 MPa. [53] The cured PDMS relaxes to 23% of its initial stiffness within 1000 s, after which it has a constant shear modulus. Assuming that the PDMS is nearly incompressible ($\nu \approx 0.5$), the associated elongation modulus was ≈10 MPa; other literature values for the elongation modulus of PDMS are closer to 1 MPa.[41,47] The material in both cases is representative of a soft polymer, compared to other such polymers as PP (1.38 GPa).[45]

The relaxation behavior of the neat PDMS is markedly different from the behavior of uncured PDMS; uncured PDMS behaves closer to a liquid with no ability to resist shear deformations as its shear modulus is six orders of magnitude lower than

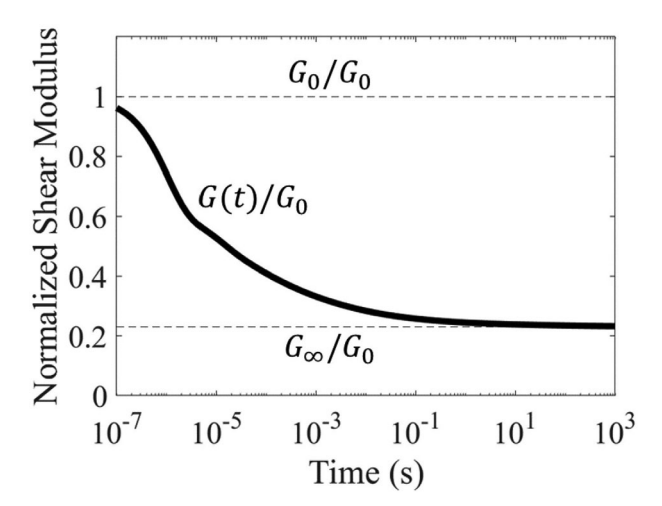


Figure 4. The viscoelastic material behavior of the normalized timedependent shear modulus for cured, neat PDMS and CNT-PDMS based on ref. [53] according to the Universal Polymer Model [57] and recharacterized for use in the 3D finite element models (FEM). The instantaneous shear modulus, G_0 , and long-term shear modulus, G_{∞} , were obtained from ref. [53] for neat PDMS and were obtained by rule of mixtures for CNT-PDMS with 3.5 wt% CNT. The relaxation behavior is described by the 20term Prony series listed in Table 1.

cured PDMS and relaxes by nearly 100% after a second of relaxation time.[16,60] Thus, cured PDMS will withstand harsh environments and retain the structured shape. The same relaxation behavior can reasonably be used for CNT-PDMS.

The rule of mixtures was used to obtain the modulus of CNT-PDMS where the elongation modulus of CNT was 1 TPa. The resulting instantaneous shear modulus for CNT-PDMS with 3.5 wt% CNT was 12 GPa; the long-term modulus was 2.7 GPa according to the relaxation behavior described in Table 1 and Figure 4. The rule of mixtures (ROM) can overpredict the modulus for CNT-filled composites because it assumes that the reinforcing material is perfectly dispersed and binds completely to the matrix material. [41,43-46] By interpolating experimental measurements of CNT-PDMS with a CNT weight content between 2 and 4 wt%, the approximate elongation modulus of PDMS with 3.5 wt% CNT is 5.7 MPa. [33] The error between the measured and predicted modulus from ROM is of the same order of magnitude as the error observed elsewhere.^[41] This overprediction is acceptable because it provides a basis for strengthening the material by the inclusion of CNTs in the PDMS matrix.

The thermo-rheological material properties of both neat PDMS and CNT-PDMS based on Equation (5) were $C_1 = 20$, C_2 = 418.86 K, and T_0 = 298 K, respectively.^[53] The reported WLF coefficients are validated by ref. [47] ($C_1 = 23.9$, $C_2 = 452.8$ K, and $T_0 = 298.1$ K), which also reports a glass transition temperature of 298.1 K. Since the reference temperature of the WLF time-temperature superposition model is the glass transition temperature of the composite, and since the temperature of the RVEs is predicted to increase in response to dynamic loading, the glassy-to-rubbery transition in the polymer does not need to be accounted for and the simplified thermo-rheological material model can be used as presented.[57,61] The same thermal conductivity was used for PDMS and CNT-PDMS, despite reports of the conductivity increasing with increasing CNT loading.[33,36]

- Acroolecular
Materials and Engineering

www.mame-journal.de

Table 2. The bounds of the three ribbing microstructural parameters, the ribbing amplitude (A), ribbing wavelength (λ), and film thickness (H) were obtained from scanning electron microscopy measurements for non-ribbed films (ribbing aspect ratio $\alpha_r = 0$) and ribbed films with a maximum ribbing aspect ratio of 0.30. Thin-films with microstructures within these bounds represent the range of possible non-ribbed and ribbed thin-film CNT-PDMS systems.

Microstructure Parameter	Lower Bound	Upper Bound
Ribbing Amplitude [mm]	0.0000	0.0500
Ribbing Wavelength [mm]	0.1667	0.7000
Film Thickness [mm]	0.2000	0.6000

4.2. Ribbing Morphology of PDMS and CNT-PDMS Thin-Films

The morphology of ribbed thin-films was obtained by SEM images from refs. [4, 16] for PDMS with 3.5 wt% CNT resulting from a parametric large-scale rolling study. The ribbing amplitude was between 0.025 and 0.045 mm; the ribbing wavelength was found to be between 0.09 and 0.62 mm; and, the thickness was between 0.30 and 0.54 mm. According to ref. [16] the ribbing aspect ratio varies between zero (non-ribbed film) and 0.30 (maximally ribbed film). These high aspect ratio topographies are difficult to achieve. [4,6,8] Some lithography techniques can obtain a minimum wavelength of only 0.150 mm^[12] and other techniques such as the multi-step imprinting compression method in ref. [59] was able to obtain a minimum wavelength on the order of 0.100 mm with alumina powder in a PVA matrix, but the maximum aspect ratio (defined as $\alpha_r = A/\lambda$) was 0.20. It is possible that the small particle size of the CNT, compared to other such fillers as alumina powder, combined with its high strength enables the creation of high aspect ratio structured surfaces.

A Latin Hypercube Sampling method was used to populate the microstructure of the 16 RVE models. To ensure that the randomly sampled microstructures stay within the range of acceptable ribbing aspect ratios, the microstructural bounds were adjusted slightly from the observed measurements, given in **Table 2**, which still capture the overall morphology of ribbing CNT-PDMS thin-films.

The combination of microstructural parameters for each of the 16 RVE thin-film models are displayed as a hypercube in **Figure 5**. Eight samples were obtained from the extreme values of Table 2; the remaining eight RVEs were sampled according to the Latin Hypercube scheme.

4.3. Ribbed Thin-Film Dynamic Thermomechanical Behavior

To isolate the effect that strain rates and material composition have on the thermomechanical response of the thin-film, the second RVE thin-film model ($H=0.479~\mathrm{mm},~A=0.046~\mathrm{mm},~\lambda=0.444~\mathrm{mm}$) subjected to a compressive strain in the parallel direction at three nominal strain rates was evaluated. The displacement in the loading direction of the second RVE for both neat PDMS and CNT-PDMS material properties was obtained in **Figure 6**.

The film subjected to the slowest nominal strain rate (10^2 s⁻¹) linearly approaches a constant displacement according to the loading profile from Figure 3, with negligible vibrations through

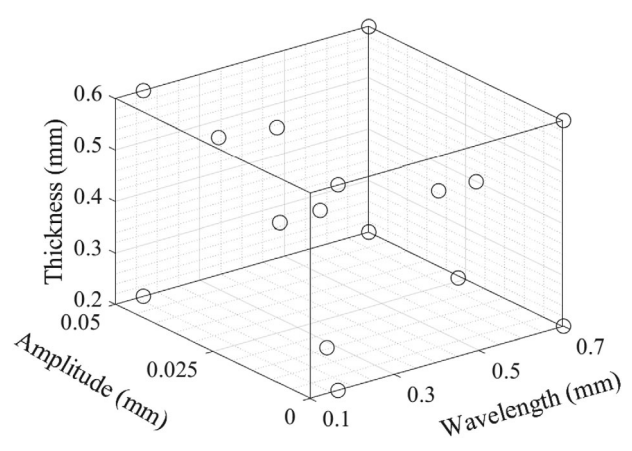


Figure 5. The microstructural parameters of the 16 representative volume element thin-film models were populated by Latin Hypercube Sampling including the eight corners within the bounds enforced by Table 2. Each circle shows the ribbing amplitude, ribbing wavelength, and film thickness of each representative volume element model in the parameter space.

the film. In the second case, the RVE is loaded at a nominal strain rate of $10^3~\rm s^{-1}$: the neat PDMS thin-film overshoots the steady-state displacement from Figure 6a before reflecting and attenuating from the viscoelastic dissipation; the CNT-PDMS thin-film exhibits the same behavior as in Figure 6a. Lastly, the PDMS film at a nominal strain of $10^4~\rm s^{-1}$ overshot the steady-state displacement by nearly two times before reflection. The observed time in Figure 6c was not long enough for the wave to reflect and show the viscoelastic relaxation, which would occur at the same rate as that in Figure 6b. The oscillatory behavior of the neat PDMS film subjected to a dynamic mechanical load resembles that of, $^{(62)}$ which showed a similar dynamic displacement response in thermo-viscoelastic materials when subjected to thermal shock—another extreme environment.

Based on the displacements in Figure 6 resulting from a parallel in-plane dynamic load, increasing the modulus of the ribbed thin-film stabilizes the film. This is apparent when considering the elastic wave speed $(c = \sqrt{E/\rho})$ of the two materials, which provides an approximate measure of the stress transmission speed through the viscoelastic medium. Using the instantaneous elongation modulus, the elastic wave speed of neat PDMS and CNT-PDMS is approximately $c_{PDMS} = 100 \text{ m s}^{-1}$ and $c_{\rm CNT-PDMS} = 6000~{\rm m~s^{-1}}$. Increasing the modulus, as in the case for CNT-PDMS, allows for stress waves to propagate through the thin-film at each time-step rather than accumulating. The wave speed in neat PDMS, however, is an order of magnitude lower than that of CNT-PDMS, so the thin-film subjected to the higher strain rates have a more complex dynamic response from the intersecting stress waves. Based on the difference between the moduli obtained from ROM and experimentally from Section 4.1, the modulus of CNT-PDMS is about three orders of magnitude larger than the experimental values. Adjusting for this would lower the wave speed to approximately $c_{\text{CNT-PDMS}} = 200 \text{ m s}^{-1}$, so minimal dynamic effects would still be seen for the highest nominal strain rate.

Each of the six stress components were also obtained from line paths through the center of the mesh in the second RVE thin-film model for neat PDMS to better understand the dynamic nature of

14392054, 0, Downloaded from https://onlinelibrary.wiley.com/doi/10.1002/mame.202400098 by North Carolina State Universit, Wiley Online Library on [30/09/2024]. See the Terms and Conditions (https://onlinelibrary.wiley

inditions) on Wiley Online Library for rules of use; OA articles are governed by the applicable Creative Commons License

www.mame-journal.de

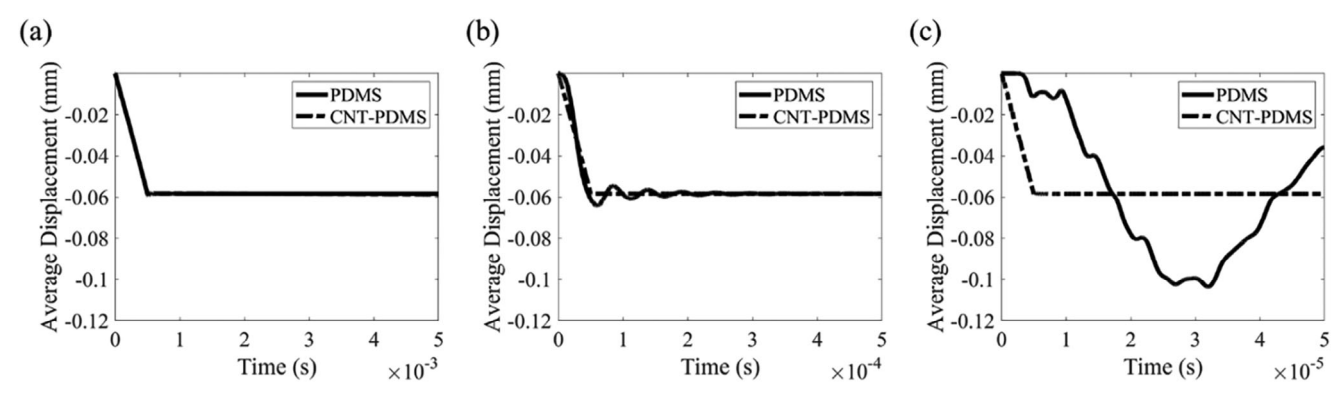


Figure 6. The average z-displacement of the line path within the thin-film model with ribbing amplitude of 0.046 mm, ribbing wavelength of 0.444 mm, and film thickness of 0.479 mm subjected to parallel loading (in the z-direction) with a nominal applied strain rate of a) 10^2 s^{-1} , b) 10^3 s^{-1} , and c) 10^4 s^{-1} .

the reflecting viscoelastic wave propagation (Figure 7). The time in Figure 7 was normalized by the total model time for easier visual comparison between the three nominal strain rates.

As with the displacements, increasing the strain rate increases the stress response and results in viscoelastic waves. Since the compressive loading is in the direction parallel to the ribbing profile (the *z*-direction), the stresses in Figure 7c are slightly larger than in Figure 7a,b. The three normal stresses (Figure 7a–c) are significantly larger than the shear stresses (Figure 7d–f). Thus, the response is governed entirely by the normal stresses. The large magnitude of the normal stresses when subjected to only 5% nominal strain at a nominal strain rate of 10⁴ s⁻¹, which is

an extreme condition. Since the strain remains below 5%, it is unlikely that additional instability modes arise, as with linearly periodic wrinkled thin-film systems.^[8,11,15]

To have a better characteristic measure of the thin-film response, the Von Mises stress normalized by the elongation modulus of the materials were obtained (Figure 8). The time was normalized by the total time.

The behavior of the neat PDMS thin-film model subjected to the three nominal strain rates is given by the solid lines in Figure 8. At a nominal strain of $10^2~\rm s^{-1}$, stress relaxation occurs immediately upon deformation and continues for the whole duration. After the RVE is loaded to the target nominal strain,

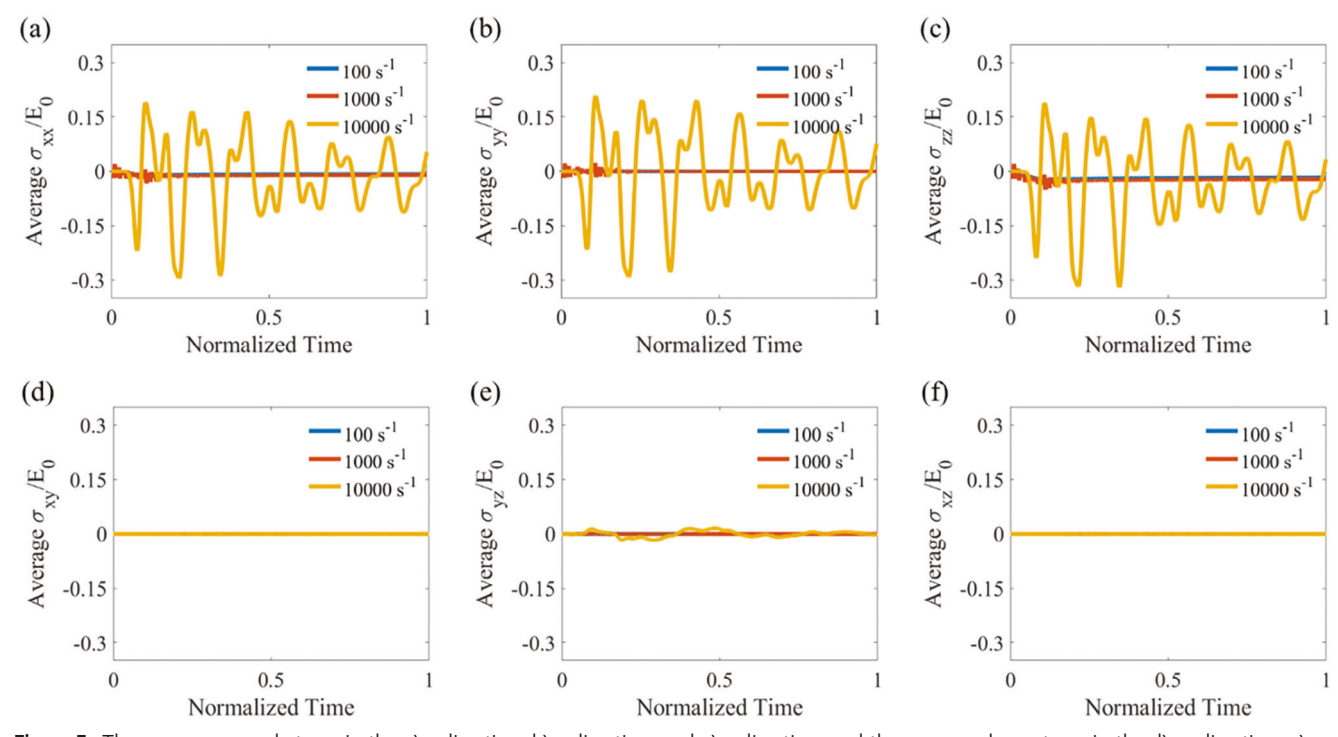


Figure 7. The average normal stress in the a) x-direction, b) y-direction, and c) z-direction, and the average shear stress in the d) xy-direction, e) yz-direction, and f) xz-direction, all normalized by the instantaneous elongation modulus of the cured, neat PDMS, E_0 , were obtained through the center path of the representative volume element model with a ribbing amplitude of 0.046 mm, ribbing wavelength of 0.444 mm, and film thickness of 0.479 mm subjected to three strain rates in the parallel ribbing direction (the z-direction).

14392054, 0, Downloaded from https://onineltbrary.wile.com/doi/10.1002/mame.202400098 by North Carolina State Universit, Wiley Online Library on [30/09/2024]. See the Terms and Conditions (https://onlinelibrary.wiley.com/terms-and-conditions) on Wiley Online Library for rules of use; OA articles are governed by the applicable Creative Commons License

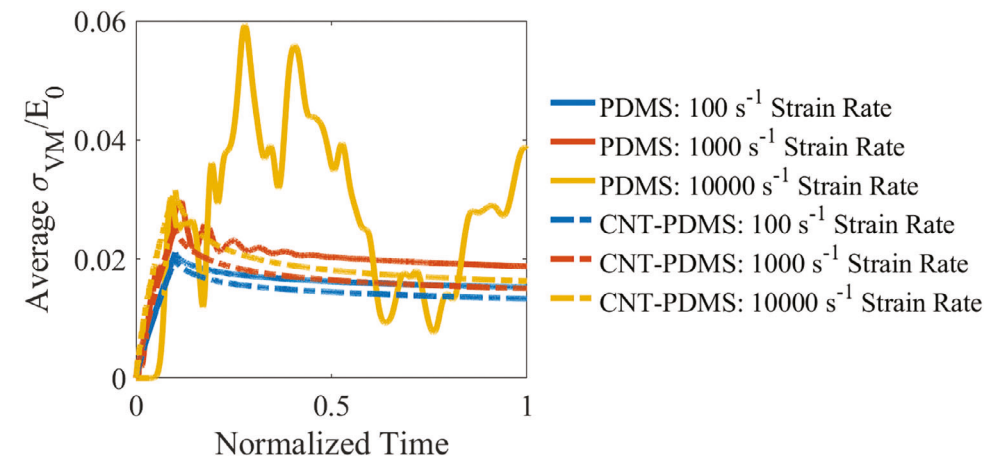


Figure 8. The average Von Mises stress normalized by the instantaneous elongation modulus of the material, E_0 , obtained from the line path within the thin-film model with ribbing amplitude of 0.046 mm, ribbing wavelength of 0.444 mm, and film thickness of 0.479 mm subjected to parallel loading. The solid and dashed lines show the behavior of neat PDMS and CNT-PDMS, respectively. The time was normalized by the total time, t_f , of each model for easier visual comparison.

the material relaxes smoothly in proportion to the long-term viscoelastic behavior. The RVE in the 103 s⁻¹ case experiences a slight overshoot in the average stress through the line path. Much like the displacements, the stress waves reflect several times as the viscoelastic material behavior dampens the response. Finally, the time delay between the displacements applied on the positive z-face and the response in the interior line path for the 10^4 s⁻¹ strain case shows the time that it takes for the viscoelastic stress waves to travel through the RVE. The interacting 3D stress wave reflections combine to triple the stress from the 10² s⁻¹ nominal strain rate case. The modeled time of 5 \times 10⁻⁵ s was not long enough to observe the stress wave relaxation based on the Prony series time constants and associated relaxation coefficients (Table 1).

Since the modulus of the thin-film structure increased by the addition of CNT inclusions, the average normalized stress response of the CNT-PDMS given by the dashed lines in Figure 8 is characteristic of a typical viscoelastic relaxation curve. Since the viscoelastic material model is rate dependent, the faster loading rate allows for less relaxation to occur than the slower rate; the maximum stress in the CNT-PDMS thin-films increases with increasing strain rate, whereas an elastic material model would be insensitive to changes in the rate of loading.

Lastly, the thermal effects of the second RVE subjected to various strain rates for the two materials was obtained (Figure 9). The initial temperature of the thin-film was 298 K; inelastic heat generation due to viscoelastic energy dissipation was the only mechanism by which the temperature of the thin-film could increase.

The heat generation is a function of the applied strain rates. It is evident in Figure 9 that the modulus of neat PDMS was too low for any temperature increase to occur. In Figure 9a, the CNT-PDMS temperature increases by 12 K during the loading phase according to Figure 3 for the 10² s⁻¹ nominal strain rate, after which the temperature remains constant. As the nominal strain rate increases, so does the increase in temperature. The 10³ s⁻¹ and 10⁴ s⁻¹ nominal strain rate cases also increase in temperature after the initial loading ramp due to the viscoelastic relaxation. The predicted temperature increase is much higher than it would be if a more experimentally-based (rather than ROMbased) modulus were used. Hence, the temperature predictions give an upper bound of the temperature increase during high strain rate loading.

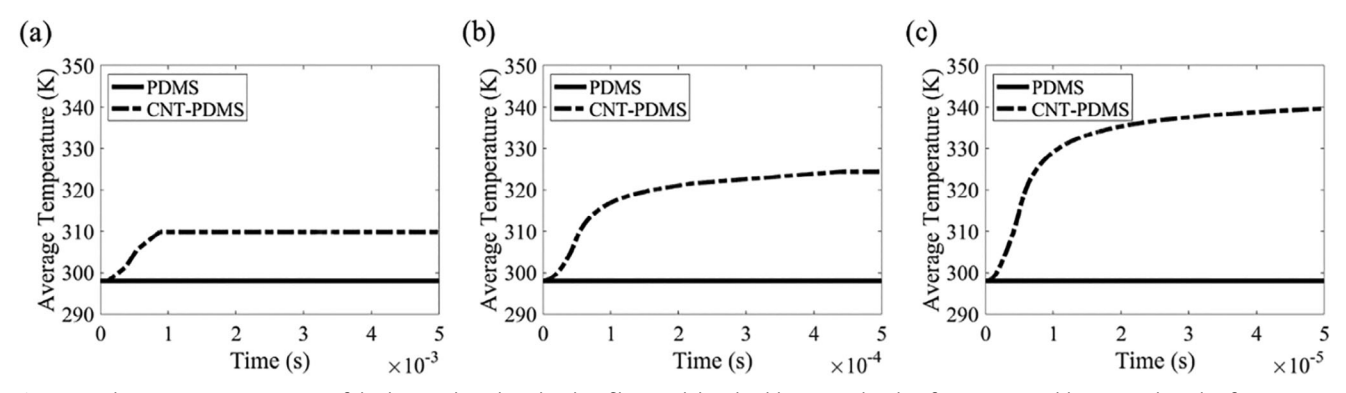


Figure 9. The average temperature of the line path within the thin-film model with ribbing amplitude of 0.046 mm, ribbing wavelength of 0.444 mm, and film thickness of 0.479 mm subjected to parallel loading with a nominal applied strain rate of a) 10^2 s⁻¹, b) 10^3 s⁻¹, and c) 10^4 s⁻¹.



www.mame-journal.de

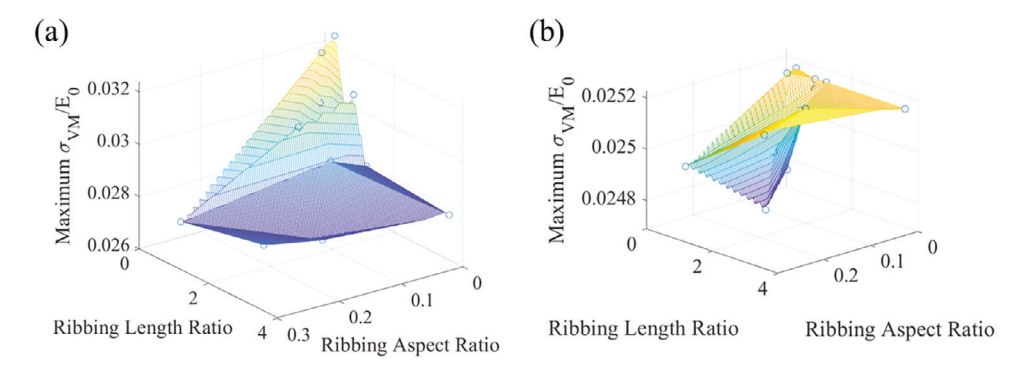


Figure 10. The maximum Von Mises stress normalized by the instantaneous elongation modulus, E_0 , for a) neat PDMS and b) CNT-PDMS obtained from each of the 16 representative volume element thin-film models subjected to a nominal strain rate of 10^3 s⁻¹. The hypersurfaces were constructed by linearly interpolating between the 16 data points obtained from FEM.

4.4. Von Mises Stress Hypersurfaces of Ribbed Thin-Films

To better understand and predict the relationship between the microstructure and the thermomechanical response, we developed hypersurfaces of the response behavior with respect to the ribbing microstructure at each nominal strain rate. The thermal responses for the remaining 15 microstructures were similar to Figure 9, and the temperature increase was not large enough to warrant concern. Instead, we focused on the mechanical response by constructing hypersurfaces of the Von Mises stress. Since we wanted to understand the behavior for extreme conditions, we obtained the maximum normalized Von Mises stress. The hypersurfaces of both PDMS and CNT-PDMS thin-films are shown in Figure 10 for a nominal strain rate of 10^3 s⁻¹. Since there are three microstructural parameters that characterize the thin-film RVE—i.e., the ribbing wavelength, ribbing amplitude, and film thickness—at least two 3D surfaces are needed to fully visualize and understand the relation between the microstructure and the resulting thermomechanical response to the dynamic loading. Instead, the two non-dimensional ribbing microstructural parameters were used: the ribbing aspect and length ratios $(\alpha_r = A/\lambda \text{ and } \alpha_l = H/\lambda).$

In Figure 10a, the stress in the neat PDMS thin-films attained the maximum value at small ribbing aspect ratios and length ratios (i.e., large wavelengths, small amplitudes, thin films). There is a large region in Figure 10a where the film stress was a minimum, which occurred at larger ribbing aspect and length ratios. It is in this region that thin-films should be designed to prevent damage when subjected to high strain rate dynamic events. CNT-PDMS thin-films subjected to a 10³ s⁻¹ nominal strain rate (Figure 10b) also show a decrease in the maximum normalized stress as a function of the ribbing aspect ratio. The maximum stress for all microstructural combinations was lower for CNT-PDMS thin-films than for neat PDMS thin-films, likely due to the reduced dynamic effects.

4.5. Ribbing Microstructure Regression Model and Uncertainty Quantification

After determining the relation between the non-dimensional microstructural parameters and the thin-film response, we wanted

Table 3. The coefficients from the regression model obtained by linear least squares to predict the maximum normalized Von Mises stress in ribbed thin-film systems with a given ribbing microstructure and nominal compressive strain rate.

	$ heta_i$	
i	PDMS	CNT-PDMS
1	3.42E-2	1.94E-2
2	2.55E-3	-2.00E-3
3	-2.07E-2	6.87E-5
4	-2.39E-2	6.14E-6
5	6.18E-3	6.13E-3
6	4.72E-3	1.30E-4
7	1.01E-5	-5.68E-6
8	-3.39E-6	-1.13E-8
9	-7.60E-7	-7.01E-9
10	4.90E-10	-4.91E-10

to understand how thin-film systems can withstand high strain rate events. A polynomial regression model was chosen to characterize the response of the thin-film with non-dimensional microstructural parameters α_l and α_r subjected to a given nominal strain rate, $\dot{\epsilon}_0$, as

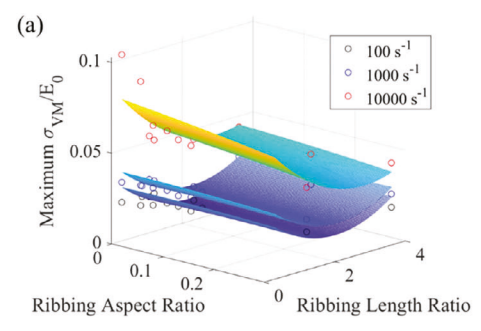
$$\frac{\sigma_{VM}(\alpha_r,\alpha_l,\dot{\epsilon}_0;\theta)}{E_0} = \theta_1 + \theta_2\alpha_r + \theta_3\alpha_l + \theta_4\alpha_r^2 + \theta_5\alpha_r\alpha_l + \theta_6\alpha_l^2
+\theta_7\dot{\epsilon}_0 + \theta_8\alpha_r\dot{\epsilon}_0 + \theta_0\alpha_l\dot{\epsilon}_0 + \theta_{10}\dot{\epsilon}_0^2$$
(6)

where θ_i is the *i*-th regression coefficient. The regression model was trained with 75% of the RVE results from all three strain rates to predict the maximum normalized Von Mises stress for a given ribbing microstructure and nominal strain rate. The remaining 25% was withheld for model testing to ensure it was not overfit. The L2-norm residual of the training data of the regression model was 0.03390 for neat PDMS and 0.00080 for CNT-PDMS; the respective residuals of the testing data were 0.02011 and 0.00087. **Table 3** shows the coefficients of the ten-term regression model for each thin-film material.

The regression model provided another method to understand how to control the topography of structured surfaces compared to the empirical relations for wrinkling given by refs. [8, 17]. The



www.mame-journal.de



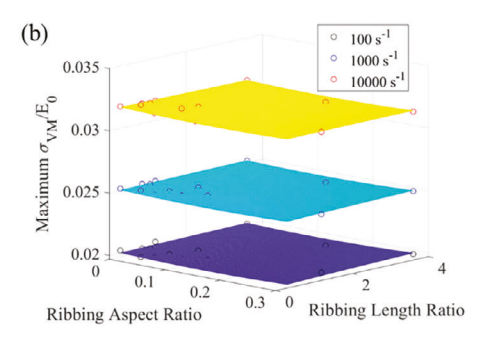


Figure 11. The maximum Von Mises stress normalized by the instantaneous elongation modulus of the material, E_0 , for a) neat PDMS and b) CNT-PDMS obtained from of each of the 16 representative volume element thin-film models for all three strain rates. The hypersurfaces were constructed for each nominal applied strain rate by the regression model obtained in Equation (6).

coefficients from Table 3 indicate that all three parameters—the non-dimensional microstructural parameters and the nominal strain rate—will have a significant effect on the maximum normalized Von Mises Stress for neat PDMS thin-films. The regression coefficients for CNT-PDMS, however, are lower for all parameters except the \dot{e}^2 -term, which suggests that the mechanical response of the higher modulus material is more dependent on the nominal strain rate than the ribbing morphology. The hypersurface of the thin-film response from a dynamic compressive load at a specified nominal strain rate can be visualized with respect to the microstructure. **Figure 11** shows the reconstructed surfaces and the RVE predictions for both materials at the three tested strain rates: $10^2 \, \mathrm{s}^{-1}$, $10^3 \, \mathrm{s}^{-1}$, and $10^4 \, \mathrm{s}^{-1}$.

The three response surfaces for neat PDMS in Figure 11a were consistent with the RVE predictions where increasing the nominal strain rate increases the predicted stress in the thin-film. They also show that there is a more significant increase in the normalized Von Mises stress for thin-films with small ribbing aspect and length ratios. The sensitivity to film thickness is also consistent with experimental observations^[51,52] and computational predictions^[13] pertaining to the high strain rate response of materials exhibiting inelastic behavior. At the higher strain rates, the thin-film was closer to the material's strength. Hence, based on our modeling predictions, thick PDMS thin-films with large ribbing amplitudes and small ribbing wavelengths are ideal for damage prevention in high strain rate dynamic events.

The response surface for CNT-PDMS (Figure 11b) shows almost no variation in the mechanical response with respect to the microstructure; rather, the response is governed almost entirely by the applied nominal strain rate as indicated by the regression model coefficients from Table 3. The magnitude of the maximum normalized Von Mises stress of neat PDMS (Figure 11a) predicted by RVE models is three times larger than that of PDMS with 3.5 wt% CNT (Figure 11b). Since the predicted stress of the CNT-PDMS thin-film RVE models is independent of the microstructure, the mechanical behavior of such CNT-PDMS thin films as those fabricated and measured to obtain the microstructural parameter bounds (Table 2) are also expected to be independent of the microstructure. Thus, the manufacturing of ribbed CNT-PDMS thin-films can be tailored to exhibit favorable surface behaviors due to high strain-rate behavior.

To further verify the neat PDMS thin-film response, the uncertainty quantification associated with the $10^4~\rm s^{-1}$ nominal strain rate was obtained in **Figure 12** to characterize the bounds of the

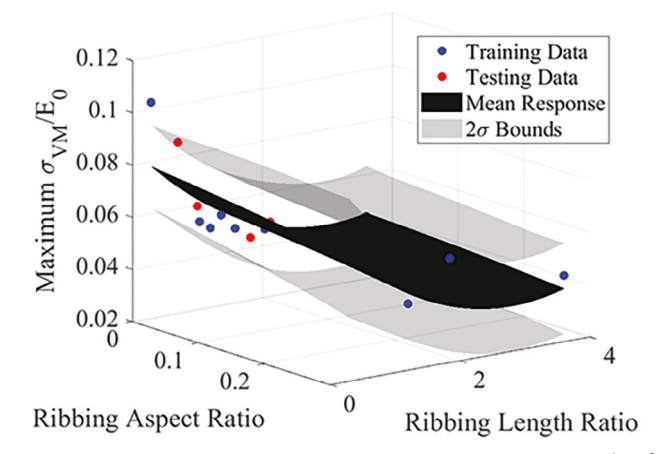


Figure 12. The uncertainty quantification associated with the $10^4 \, \mathrm{s^{-1}}$ strain rate models for neat PDMS trained with 75% of the FEM predictions and tested with the remaining 25%. The mean response from the regression model at a strain rate of $10^4 \, \mathrm{s^{-1}}$ and the 2-standard deviation bound surfaces are included.

regression surface.

Figure 12 shows the uncertainty in the regression model predictions at the higher strain rate, which is important to understand the predictive capabilities of the model for the high strain rate regime. Almost all the training and testing data provided from the RVEs reside within the surfaces created by the standard deviation, and since the distance between those surfaces is reasonably narrow the regression model can serve as a guide for predicting the stress in thin-films with a prescribed microstructure subjected to a compressive load.

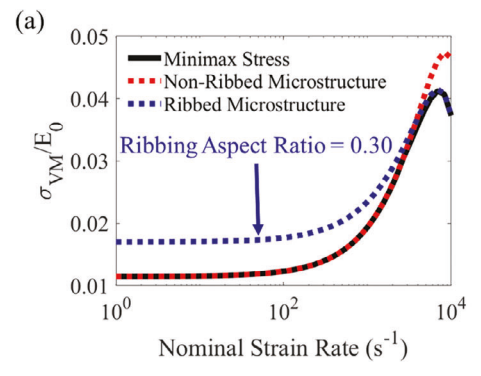
4.6. Ribbing Microstructure Optimization for Thin-Film Design

Since the regression model is representative of the behavior of the hypersurfaces created by the population of RVEs sampled by the Latin Hypercube method, it can be used to optimize the microstructure and predict the thin-film response to dynamic loading for various compressive loadings. A constrained interior-point optimization routine was used and evaluated for nominal strain rates between 10° and 10⁴ s⁻¹. For each strain rate, the minimax normalized Von Mises stress was obtained with the corresponding microstructure (**Figure 13**). The optimization





www.mame-journal.de



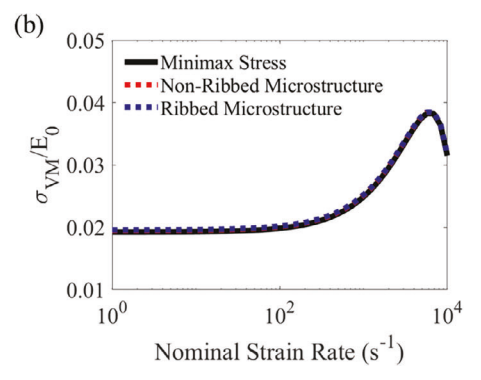


Figure 13. The regression model was optimized to obtain the microstructure yielding the lowest maximum stress (minimax stress) for a) neat PDMS and b) CNT-PDMS. The solid black curve gives the minimax stress of all microstructural combinations for nominal strain rates between 10^0 s^{-1} and 10^4 s^{-1} . The dashed red and blue curves give the minimax stress for a non-ribbed film ($\alpha_r = 0$) and a maximally ribbed film ($\alpha_r = 0.30$), respectively.

procedure was twice repeated for each material with a constant ribbing aspect ratio of 0 (non-ribbed film) and of 0.3 (maximally ribbed film) to understand how the two film types behave.

Below strain rates of 10² s⁻¹, the response of the neat PDMS thin-film approaches quasi-static behavior, based on the regression model predictions in Figure 13a. In this regime, ribbed thin-films have a maximum stress 1.5 times larger than a nonribbed film. Above the quasi-static strain rate, the maximum stress in the ribbed and non-ribbed films increased. After a nominal strain rate of 1200 s⁻¹ (Figure 13a), a neat PDMS ribbed film outperforms the non-ribbed film and attained the minimax value. Higher strain rate regimes are critical for design considerations because the predicted stress increased as the strain rate increases.^[50,52] Given that the nominal strain was only 5% in these RVE models, all the thin-films are still far from failure since they are in the linear viscoelastic regime; but for larger nominal strains, as the predictions indicate, failure would be most likely to occur in a non-ribbed film than in a ribbed film.

In contrast, the behavior of CNT-PDMS is insensitive to changes in microstructure. Based on the minimax stress of CNT-PDMS and PDMS systems (solid black line in Figure 13a,b), there is little difference in the optimal performance of neat PDMS and CNT-PDMS. The advantage that CNT-PDMS has over neat PDMS is that this minimax value is attainable for any ribbing microstructure, while it is only achieved for specific microstructures in PDMS. Thus, the design of ribbed CNT-PDMS thin-films can be focused on maximizing other favorable surface behaviors, such as drag reduction, superhydrophobicity, and antifouling.

5. Summary

A nonlinear explicit dynamic FE scheme was used with a viscoelastic material model subjected to compressive high strain rates and inelastic heat generation to understand and predict the thermomechanical response of ribbed thin-film structures manufactured by large-scale rolling. The shear and elongation moduli of the CNT-PDMS were determined by the rule of mixtures. The dynamic response of neat PDMS was also modeled, based on a Prony series representation, to understand how the high strength CNT inclusions affects the thermomechanical re-

sponse. The RVE models of the ribbed thin-films were subjected to dynamic nominal strain rates in both the transverse and parallel ribbing directions, with strain rates as high as $10^4 \, {\rm s}^{-1}$. Latin Hypercube Sampling of the microstructural parameters, as informed from experimental observations and measurements, provided physically realistic microstructurally-based RVEs.

For the CNT-PDMS ribbed thin-films, the thermomechanical response is directly related to the effects of the nominal strain rate. At the lower strain rate of $10^2\ s^{-1}$, the temperature of the CNT-PDMS thin-films increases by only 12 K. At the higher strain rate of 10^4 s⁻¹, the temperature increased by \approx 40 K. For the mechanical behavior, as the nominal strain rate increases from 10^2 to 10^4 s⁻¹, the maximum values of the Von Mises stress almost increases by a factor of two. The CNT-PDMS thin-film structures rapidly attained steady-state behavior after the initial viscoelastic relaxation. The mechanical response of neat PDMS, in contrast, is highly dependent on both the ribbing microstructure and the nominal strain rate. There was a transition region at a nominal applied strain rate of 1200 s⁻¹ where the wave speed of the material is lower than the nominal loading velocity due to wave interactions resulting in a significant increase in stress. The non-ribbed films have lower maximum stresses for nominal strain rates lower than 1200 s⁻¹, but highly ribbed films are advantageous for strain rates higher than 1200 s⁻¹ because they impede the interacting stress waves. There is no significant temperature increase in neat PDMS thin-films for the modeled strain rates because the modulus is too low for sufficient heat to be generated, regardless of the ribbing microstructure. By strengthening the material with CNTs, there were reductions in stress wave interactions due to the different material constituents, which lowers the resulting film stress but increases the film temperature for all ribbing morphologies.

The interior-point optimization routine was based on a regression model trained from the FE predictions to design ribbed materials for multifunctional applications. The model validates that CNT inclusions can be used to mitigate damage in thin-film materials subjected to dynamic compressive loadings by resulting in lower stresses. The ribbing morphology can, therefore, be used to understand and control surface behavior, such as superhydrophobicity, drag reduction, or antifouling, without compromising the desired mechanical behavior of the film.





www.mame-journal.de

Acknowledgements

The authors were all supported by the National Science Foundation grant no. 2031558.

Conflict of Interest

The authors declare no conflict of interest.

Data Availability Statement

The data that support the findings of this study are available on request from the corresponding author. The data are not publicly available due to privacy or ethical restrictions.

Keywords

carbon nanotubes, high strain rate, Latin hypercube, microstructural design, polymers, ribbing, thermo-rheological

Received: March 14, 2024 Revised: June 12, 2024 Published online:

- J. Ryu, K. Kim, J. Park, B. G. Hwang, Y. Ko, H. Kim, J. Han, E. Seo, Y. Park, S. J. Lee, Sci. Rep. 2017, 7, 1981.
- [2] C. Yang, F. Wang, W. Li, J. Ou, C. Li, A. Amirfazli, Appl. Phys. A 2016, 122. 1.
- [3] Y. Sun, Z. Yang, L. Li, Z. Wang, Q. Sun, J. Membr. Sci. 2019, 581, 224.
- [4] M.d D. Islam, H. Perera, B. Black, M. Phillips, M.-J. Chen, G. Hodges, A. Jackman, Y. Liu, C.-J. Kim, M. Zikry, S. Khan, Y. Zhu, M. Pankow, J. E. Ryu, Adv. Mater. Interfaces 2022, 9, 2201237.
- [5] C. Guo, Q. Tian, H. Wang, J. Sun, L. Du, M. Wang, D. Zhao, Micro Nano Lett. 2017, 12, 439.
- [6] S.-H. Park, S. Lee, D. Moreira, P. R. Bandaru, I. Han, D.-J. Yun, Sci. Rep. 2015, 5, 15430.
- [7] L. Cao, A. K. Jones, V. K. Sikka, J. Wu, D. Gao, Langmuir 2009, 25, 12444
- [8] N. Liu, Q. Sun, Z. Yang, L. Shan, Z. Wang, H. Li, Adv. Sci. 2023, 10, 2207210.
- [9] M. J. Imburgia, A. J. Crosby, Extreme Mech. Lett. 2016, 6, 23.
- [10] Q. Xu, W. Zhang, C. Dong, T. S. Sreeprasad, Z. Xia, J. R. Soc. Interface 2016, 13, 20160300.
- [11] F. Xu, M. Potier-Ferry, Sci. Rep. 2017, 7, 18081.
- [12] D. Kim, K.-S. Yun, Microsyst. Technol. 2013, 19, 743.
- [13] H. Shang, X. Liang, F. Deng, S. Hu, S. Shen, Int. J. Mech. Sci. 2022, 234, 107685.
- [14] T. Sharma, Y. Vamsi Krishna, A. Kumar, Mater. Today Proc. 2021, 46, 5530.
- [15] S. Nikravesh, D. Ryu, Y.-L. Shen, Sci. Rep. 2021, 11, 16449.
- [16] M. Phillips, M.-J. Chen, M. D. Islam, J. Ryu, M. A. Zikry, Adv. Eng. Mater. 2023, 25, 2300582.
- [17] A. Schweikart, A. Fery, Microchim. Acta 2009, 165, 249.
- [18] R. J. Fields, M. F. Ashby, Philos. Mag. 1976, 33, 33.
- [19] J. S. Biggins, L. Mahadevan, Soft Matter 2018, 14, 7680.
- [20] D. J. Coyle, C. W. Macosko, L. E. Scriven, J. Fluid Mech. 1990, 216, 437.
- [21] M. Decré, E. Gailly, J.-M. Buchlin, Phys. Fluids 1995, 7, 458.
- [22] M. D. Graham, Phys. Fluids 2003, 15, 1702.
- [23] M. E. G. Castillo, A. T. Patera, J. Fluid Mech. 1997, 335, 323.

- [24] C.-H. Chien, J.-Y. Jang, J. Mech. Sci. Technol. 2007, 21, 1892.
- [25] T. Hasegawa, K. Sorimachi, AIChE J. 1993, 39, 935.
- [26] J. P. Mmbaga, R. E. Hayes, F. H. Bertrand, P. A. Tanguy, Int. J. Numer. Methods Fluids 2005, 48, 1041.
- [27] J. Nase, A. Lindner, C. Creton, Phys. Rev. Lett. 2008, 101, 074503.
- [28] G. A. Zevallos, M. S. Carvalho, M. Pasquali, J. Non-Newton Fluid Mech. 2005, 130, 96.
- [29] C. Daniel, D. Wood III, G. Krumdick, M. Ulsh, V. Battaglia, P. R. Schunk, F. Crowson, Roll-to-Roll Advanced Materials Manufacturing DOE Laboratory Collaboration (FY2020 Final Report), U. S. Department of Energy, Washington, DC 2021.
- [30] J. H. Lee, J. C. Hyun, Korea-Aust Rheol J 2010, 22, 75.
- [31] M. M. Rahman, S. Zainuddin, M. V. Hosur, J. E. Malone, M. B. A. Salam, A. Kumar, S. Jeelani, Compos. Struct. 2012, 94, 2397.
- [32] F. Wang, L. T. Drzal, Y. Qin, Z. Huang, J. Mater. Sci. 2016, 51, 3337.
- [33] J. Du, L.i Wang, Y. Shi, F. Zhang, S. Hu, P. Liu, A. Li, J. Chen, Sensors 2020, 20, 4523.
- [34] J. Cai, M. Huang, X. Chen, M. Wang, J. Appl. Polym. Sci. 2022, 139, 52113.
- [35] H. Xu, L.i-X. Gong, X.u Wang, L.i Zhao, Y.-B. Pei, G. Wang, Y.a-J. Liu, L.-B. Wu, J.-X. Jiang, L.-C. Tang, Compos. Part Appl. Sci. Manuf. 2016, 91, 53.
- [36] B. Zhou, W. Luo, J. Yang, X. Duan, Y. Wen, H. Zhou, R. Chen, B. Shan, Compos. Part Appl. Sci. Manuf. 2016, 90, 410.
- [37] Y.-T. Li, W.-J. Liu, F.-X. Shen, G. D. Zhang, L.-X. Gong, L. Zhao, P. Song, J.-F. Gao, L.-C. Tang, Compos. Part B Eng. 2022, 238, 109907.
- [38] A. Lapinska, N. Grochowska, J. Antonowicz, P. Michalski, K. Dydek, A. Duzynska, A. Daniszewska, M. Ojrzynska, K. Zeranska, M. Zdrojek, Sci. Rep. 2022, 12, 19038.
- [39] F. T. Fisher, L. C. Brinson, Compos. Sci. Technol. 2001, 61, 731.
- [40] S. Kamarian, M. Shakeri, M. H. Yas, Polym. Compos. 2018, 39, 1433
- [41] A. T. Sepúlveda, R. Guzman de Villoria, J. C. Viana, A. J. Pontes, B. L. Wardle, L. A. Rocha, *Nanoscale* 2013, 5, 4847.
- [42] A. H. Esbati, S. Irani, Mech. Mater. 2018, 118, 106.
- [43] S. Yang, S. Yu, W. Kyoung, D.o-S. Han, M. Cho, Polymer 2012, 53, 623.
- [44] S. Yang, S. Yu, J. Ryu, J.-M. Cho, W. Kyoung, D.o-S. Han, M. Cho, Int. J. Plast. 2013, 41, 124.
- [45] M. A. Bhuiyan, R. V. Pucha, J. Worthy, M. Karevan, K. Kalaitzidou, Comput. Mater. Sci. 2013, 79, 368.
- [46] Z. Liu, J. A. Moore, S. M. Aldousari, H. S. Hedia, S. A. Asiri, W. K. Liu, Comput. Mech. 2015, 55, 963.
- [47] R. Song, H. Schrickx, N. Balar, S. Siddika, N. Sheikh, B. T. O'Connor, Macromolecules 2020, 53, 1988.
- [48] H. He, J. Liu, Y. Zhang, X. Han, W. V. Mars, L. Zhang, F. Li, *Polymers* 2022, 14, 2210.
- [49] M. O. Tas, M. A. Baker, M. G. Masteghin, J. Bentz, K. Boxshall, V. Stolojan, ACS Appl. Mater. Interfaces 2019, 11, 39560.
- [50] J. S. Kim, H. Huh, Exp Mech 2011, 51, 845.
- [51] E. Ben-David, T. Tepper-Faran, D. Rittel, D. Shilo, Exp. Mech. 2014, 54, 1687.
- [52] E. Ben-David, T. Tepper-Faran, D. Rittel, D. Shilo, Scr. Mater. 2014, 90–91, 6.
- [53] K. Long, J. Brown, A Linear Viscoelastic Model Calibration of Sylgard 184, U. S. Department of Energy, Washington, DC 2017.
- [54] ABAQUS/Standard User's Manual, Version 6.9 Dassault Systemes Similia Corp. https://abaqus-docs.mit.edu/2017/English/SIMACAEEXCRefMap/simaexc-c-docproc.htm (accessed: January 2023).
- [55] H. Asadian, K. Shelesh-Nezhad, Polym. Compos. 2020, 41, 817.
- [56] R. W. Mailen, Y. Liu, M. D. Dickey, M. Zikry, J. Genzer, Soft Matter 2015, 11, 7827.





www.mame-journal.de

- [57] D. B. Adolf, R. S. Chambers, M. A. Neidigk, *Polymer* 2009, 50, 4257.
- [58] M. L. Williams, R. F. Landel, J. D. Ferry, J. Am. Chem. Soc. 1955, 77, 3701.
- [59] T. Miyata, K. Tokumaru, F. Tsumori, Jpn. J. Appl. Phys. 2020, 59, SIIJ07.
- [60] S. Marceau, P. Dubois, R. Fulchiron, P. Cassagnau, Macromolecules 2009, 42, 1433.
- [61] U. D. Çakmak, F. Hiptmair, Z. Major, Mech. Time-Depend. Mater. 2014, 18, 139.
- [62] M. F. Oskouie, R. Ansari, H. Rouhi, Mech. Adv. Mater. Struct. 2020, 27, 800.